



Correlation between microstructure and mechanical properties of welding joint in 9% Ni steel with two types of Ni-based superalloy filler metals

Ji Yong Hwang¹ · Kwangsu Choi^{1,2} · Hyo Yun Jung¹

Received: 6 July 2022 / Accepted: 31 August 2022 / Published online: 8 September 2022
© The Author(s), under exclusive licence to Springer-Verlag London Ltd., part of Springer Nature 2022

Abstract

Flux-cored arc welding (FCAW) joints with 9% Ni steel were prepared using Ni-based superalloy filler metals. The correlation between the microstructure and mechanical properties of the weld joint based on the type of filler materials was investigated. Owing to the heat transferred during the welding process, the heat-affected zone (HAZ) of the base metal primarily comprised martensite and exhibited higher hardness than the weld metal and existing base metal. To evaluate the toughness of FCAW joints against low-temperature fractures, Charpy impact tests at $-196\text{ }^{\circ}\text{C}$ were conducted; an absorbed impact energy of at least 55 J was observed in the weld metal, HAZ, and base metal regions, which was significantly higher than the standard specification. Comparing Alloys 709 and 609 as filler metals, a higher absorbed impact energy was observed when using Alloy 709 in both the weld metal and HAZ regions. This is because the quantity of precipitates, which can act as a point of crack initiation and propagation in weld beads, was smaller when Alloy 709 was used, and the γ phase was stably maintained even at low temperatures owing to the high content of elements that decrease the martensite start temperature (γ stabilizers) in the bead and transition areas. Furthermore, Alloy 709 obtained a low volume fraction and small grain size in the coarse-grained HAZ, which is known as the toughness degradation zone. This can contribute to the higher impact toughness compared with Alloy 609.

Keywords 9% Ni steel · Ni-based superalloy · Microstructure · Mechanical property · Flux-cored arc welding

1 Introduction

Because 9% Ni steel exhibits excellent fracture toughness even at extremely low temperatures, it is used for liquefied natural gas (LNG) storage tanks [1–4]. To meet the strict sulfur oxide emission regulations, LNG-propulsion ships that use eco-friendly natural gas as the main fuel have been gaining attention recently [5, 6]. As a result, research regarding 9% Ni steel used in LNG storage tanks and the corresponding welding technology is ongoing.

According to the data reported by Berejnoi and Ipiña, the stability of materials at various temperatures varies with the crystalline structure [7]. The body-centered cubic (BCC) structure undergoes rapid changes in ductility and brittleness with temperature, whereas the face-centered cubic (FCC) structure has constant absorbed impact energy even at low temperatures, and appears to be more suitable for extremely low-temperature environments. Because LNG has a very low liquefaction temperature ($-162\text{ }^{\circ}\text{C}$), it is essential that storage tanks function stably without damage even at extremely low temperatures [3, 4]. Therefore, 9% Ni steel used for LNG tanks is formed by adding Ni to induce the formation of austenite (γ , FCC), thereby forming a duplex structure of martensite and austenite [8, 9].

For 9% Ni steel, Ni-based alloys with an austenitic structure are used as filler metals to impart low-temperature stability. In the welding process of 9% Ni steel (Fe-based alloy) with a Ni-based filler metal, changes occur in the composition and microstructure of the joint area. First, in the case of the dilution (transition) area in which the two alloys are

✉ Hyo Yun Jung
hjung@kitech.re.kr

¹ 3D Printing Manufacturing Process Center, Advanced Forming Process R&D Group, Korea Institute of Industrial Technology, 40, Techno saneop-ro 29 beon-gil, Ulsan, Republic of Korea 44776

² Department of Materials Science and Metallurgical Engineering, Kyungpook National University, 80, Daehak-ro, Daegu, Republic of Korea 41566

Table 1 Chemical composition of 9% Ni steel (wt. %)

	Fe	Ni	C	Si	Mn	P	S
9% Ni steel	Bal	8.860	0.060	0.250	0.600	0.007	0.001

mixed, the elemental distribution and microstructure of the area affects low-temperature impact toughness; this was confirmed through a preliminary study on the microstructural differences in the dilution area based on the type of filler metals [10]. In a study by Kim et al. the transition zone was observed near the fusion line, and the compositional changes and microstructural evolution in the area were reported [11]. Mu et al. discussed the formation of martensite in the dilution zone, which results in the acceleration of crack propagation and degradation of impact toughness [12]. Thus, it was determined that the microstructure of the dilution zone is directly related to the mechanical properties of the weld metals. In contrast, the heat-affected zone (HAZ) represents the base metal region affected by the heat transferred during welding, and is located directly under the weld metal. Because of the transferred heat, the HAZ experiences microstructural changes, and a weak region can develop [13–17]. Because the initiation and propagation of cracks in the HAZ can result in fractures, the corresponding microstructural characteristics and mechanical behavior must be studied [2, 9, 13].

The shielded metal arc welding (SMAW) method is commonly applied for the welding of 9% Ni steel, except in some cases of horizontal welding [1, 4]. However, SMAW is a manual process; hence, the quality of the weld significantly depends on the skill level of the operator. The welding efficiency, which reflects how quickly the welding process can deposit the filler metal, is as low as about 60% in the case of SMAW because it cannot continuously supply the filler metal. The deposition efficiency, which measures the actually deposited filler metal compared to the molten filler metal, is also low at 55–75%, and the process cost increases with the stub loss of the filler metal [18, 19]. In contrast, flux-cored arc welding (FCAW) is a semiautomatic or automatic process with a continuous supply of the filler metal. It has the advantages of high welding efficiency (80–85%), deposition efficiency (80–90%), and improved productivity. Therefore, FCAW achieves more consistent welding quality compared to SMAW, and has been investigated as an alternative technology with promising results [19]. However,

despite the knowledge that the microstructure and compositional distribution are important factors for determining mechanical properties, few studies on FCAW joints and different types of filler metals have been conducted.

In this study, the filler metals Alloys 709 and 609 were subjected to bead-on-plate welding of 9% Ni steel using the FCAW method. Alloy 709, for which insufficient research results exist, was used as the main filler metal for FCAW welding of 9% Ni steel, and the microstructure and mechanical properties of the joint were compared to those of Alloy 609. To this end, the microstructure differences in the bead, transition area, and HAZ based on the filler metal were analyzed, and the correlation between the microstructure and mechanical properties was investigated.

2 Experimental methods

The chemical compositions of 9% Ni steel (Nippon Steel & Sumitomo Metal Corporation) and filler metals (Alloy 709 and Alloy 609) are listed in Tables 1 and 2.

The filler metals used were flux-cored wire (FCW) with a 1.2 mm diameter, and the corresponding cross-sectional images and elemental mapping results are shown in Fig. 1.

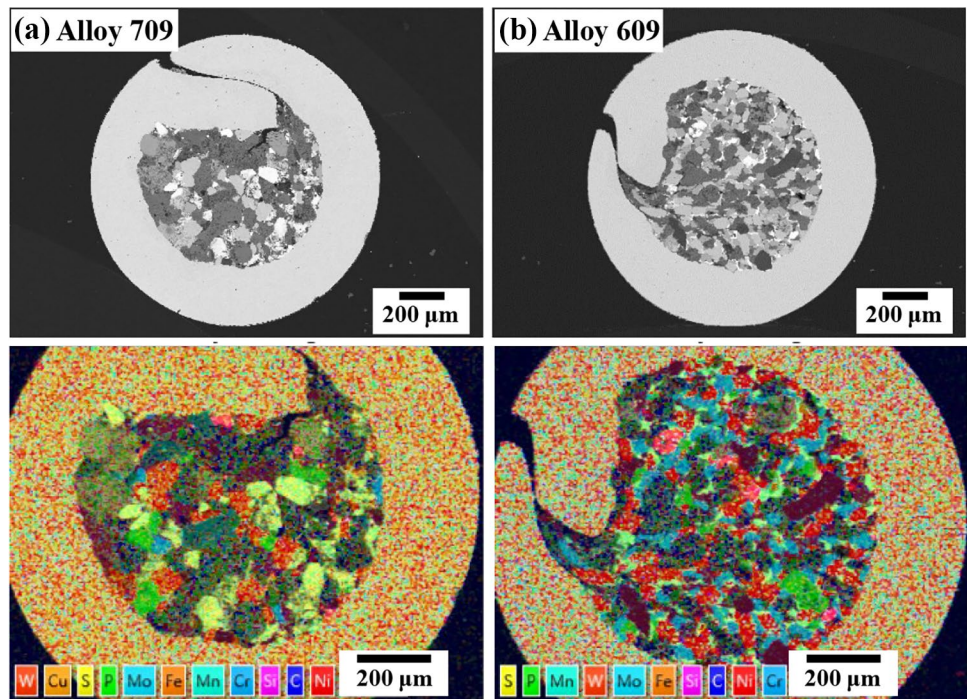
Single beads of each filler metal were prepared using the FCAW method. The shapes of the bead and HAZ region, penetration depth, and hot cracking were investigated based on the current and scan speed of the FCAW welding. The welding conditions are listed in Table 3.

The microstructure was analyzed for the weld bead, transition region, and HAZ based on the filler metal type. The microstructure observation was performed through optical microscopy (OM, HiROX, MXB-5000REZ, Japan) and field emission-scanning electron microscopy (FE-SEM, Hitachi, SU8230, Japan). Composition analysis was performed for each region of the weld joint through point and line analysis using energy-dispersive spectrometry (EDS, Oxford, Ultim Max100, UK). The hardness was measured with a Vickers hardness tester (EMCO-TEST, Durajet, Austria) under a load of 2.942 N. Hardness measurements were performed

Table 2 Chemical compositions of filler metals (wt. %)

Filler metal		Ni	Cr	Mo	Fe	W	Si	Mn	C	Cu	P	S
DW-N709SP (ENiMo13T1-1/4)	Alloy 709	Bal	6.700	17.200	6.800	2.600	0.120	2.400	0.010	0.010	0.012	0.003
DW-N609SV (-)	Alloy 609	Bal	15.700	16.200	6.600	3.300	0.270	0.270	0.010		0.012	0.002

Fig. 1 SEM images and EDS mapping results of flux-cored wires of **a** Alloy 709 and **b** Alloy 609



at regular intervals in the diagonal direction from the weld to the base metal across the fusion line. To evaluate the low-temperature toughness, multi-layer welded samples were prepared to conduct Charpy V-notch impact tests in a cryogenic environment at $-196\text{ }^{\circ}\text{C}$. A V-notch with a 2-mm depth was formed on the multi-layer welded sample, and the impact absorption energy was measured for each weld metal and HAZ region. A schematic diagram is shown in Fig. 2.

3 Results and discussion

A single bead was formed using Alloys 609 and 709, which are Ni-based filler metals, on 9% Ni steel. Figure 3 shows cross-sectional OM images of the weld beads with the dimensions of the HAZ regions. The observation was

Table 3 Welding conditions for 9% Ni Steel and Ni-based filler metals

Welding parameters	
Welding machine	CMT/KUKA
Base metal	9% Ni steel
Filler metal (wire)	Ni-based alloy (Alloy 709, Alloy 609)
Shield gas	Ar-18% CO ₂
Welding current	200 A
Welding speed	20 cm/min

performed closely from the weld metal to the HAZ region, including the joint interface.

3.1 Microstructure of weld metal

Figure 4 shows SEM images for each weld metal region using Alloy 709. In the case of the weld metal with Alloy 709, five regions can be observed in the direction from the top of the bead (Fig. 4a) toward the fusion line (Fig. 4e), and a microstructural transition is exhibited depending on location within the welding bead. The top region of the Alloy 709 bead in Fig. 4a shows the formed equiaxed dendrites, whereas the lower region (Fig. 4b) exhibits columnar dendrites. Subsequently, the directional columnar–dendrite (Fig. 4c) and dendrite–cellular transition forms (Fig. 4d) can be observed closer to the bottom, and planar morphology (Fig. 4e) can be seen immediately above the fusion line. The formation of precipitates is observed in the boundary region between the grains. At the boundary of the equiaxed dendrite, several precipitates with a relatively large size of $\sim 8\text{ }\mu\text{m}$ are observed, and the number and size of the precipitates tend to decrease according to the microstructure transition from the equiaxed dendrite to the cellular morphology. No precipitates are observed in the planar growth region.

Figure 5 shows SEM images of the weld metal region with Alloy 609. A microstructural transition can be observed from the top of the bead to the bottom, which is similar to the case of Alloy 709 (Fig. 5a–e). Therefore, the microstructural

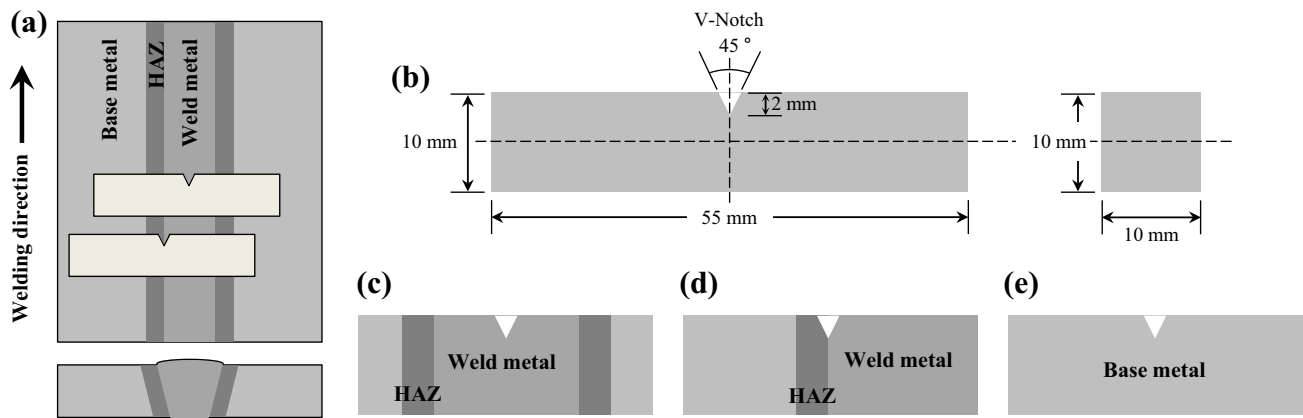


Fig. 2 Schematic diagram of **a** sampling location for Charpy impact test, **b** size of impact test specimen, and **c** weld metal, **d** HAZ, and **e** base metal notch location

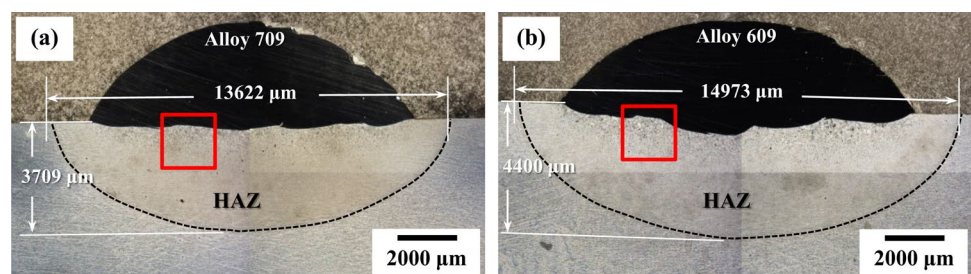
change showed the same trend, regardless of the weld metal type. Thus, it can be assumed that in this study, the composition of the filler metal does not have a significant effect on the microstructure of the weld bead.

The microstructural transition appears to depend on the correlation between the temperature gradient (G) of the melt pool and the crystal growth rate (R) during solidification, and the same trend has been reported in our previous study [10]. G is the tangent of the melt pool temperature profile as a function of distance, and R is defined as the moving speed of the solid–liquid interface. The preferred solidification morphology depends on the G/R ratio. At low G/R , which is a high crystal growth rate and a low temperature gradient, equiaxed dendrites are formed. As R decreases and G increases (higher G/R), the microstructure changes from equiaxed dendrite, through columnar dendrite, cellular dendrite, and cellular, to planar growth [20, 21]. The bead bottom, which is rapidly cooled because it is in contact with the cold base material, has a high G and a low R . As a result, the bottom part near the joint interface shows the planar/cellular morphology. Nearer the top of the bead, there is less heat extraction. Thus, the cooling rate is reduced, resulting in a low G and a high R . This can explain why the microstructure toward the bead top exhibits a transition from cellular, through columnar, to equiaxed dendrites. Farias et al. reported dendrite to planar growth in an AWS ER NiCrMo-3

sample clad by the gas tungsten arc welding (GTAW) method [22]. Additionally, a similar microstructural transition was observed during the solidification of other alloys, such as the GH909 superalloy [23], Al–Mg–Si [24], and Al–Zn [25].

Based on the findings of previous studies and the Ni–Cr–Mo ternary phase diagram [26–28], the solidification behavior of the two weld metals can be explained as follows: the primary γ phase (dendrite) is formed, and the residual liquid (interdendritic area) is solidified in the surrounding area, causing precipitates to develop. The equilibrium composition of the primary γ phase changes with decreasing temperature due to solidification. According to the Ni–Cr–Mo phase diagram calculated by Turchi et al. [29], the Mo content for stable γ decreases significantly compared to Ni and Cr content as the temperature decreases. From this, it can be seen that when the temperature decreases during the solidification process, the equilibrium composition of γ indicates a low Mo content. Therefore, depending on the equilibrium composition of γ with temperature, the excess elements diffuse into the surrounding liquid phase. The compositional analysis of each structure (Table 4) shows that the interdendritic region was richer in Mo than the dendrite region, indicating Mo rejection in the residual liquid during the primary phase solidification. The Mo segregation results in the secondary

Fig. 3 Cross-sectional OM images of weld bead of **a** Alloy 709 and **b** Alloy 609



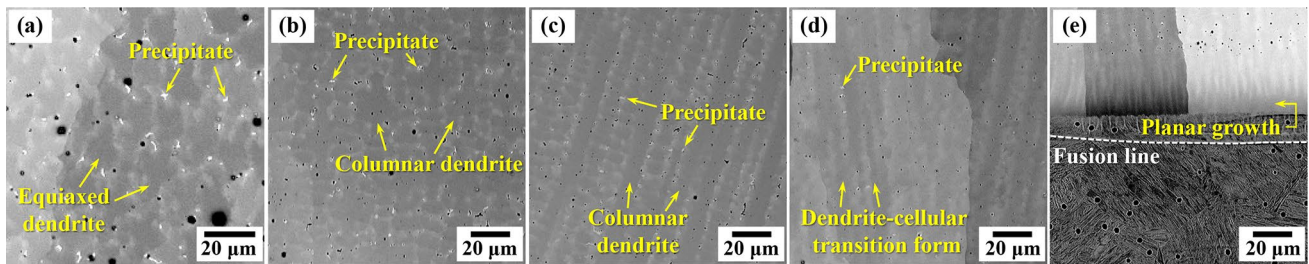


Fig. 4 SEM images with the position within Alloy 709 weld bead. The microstructure in the direction toward the joint interface from bead top is shown in the order of **a** to **e**: weld bead **a** top, **b**, **c** middle, **d** bottom, and **e** joint interface

phase formation, and a high Mo content was measured in the corresponding precipitates.

From the reported compositional analysis results and their comparison, the precipitates were found to be the ρ phase [27, 30]. Perricone et al. reported a Ni–Cr–Mo ternary liquidus projection through a computational thermodynamic algorithm-based calculation for solidification [26]. Figure 6 shows the liquidus projection according to the alloying element used. The ρ and σ phase regions tend to increase with the addition of Fe and W. Particularly, it can be seen that W expands and stabilizes in the ρ phase region. This is consistent with the high W content in the precipitates of Alloys 709 and 609 weld metals obtained in this study, and supports the ρ phase formation. In summary, the composition of Ni, Cr, and Mo, which are the main elements of Alloys 709 and 609, induces the formation of the primary γ phase. Depending on the equilibrium composition of γ , excess Mo and W diffuse into the surrounding liquid phase, and segregation of Mo and W leads to the formation of ρ . A schematic diagram of the solidification behavior was presented in our previous study [10].

These precipitates occur owing to the segregation of Mo and W through rejection around the dendrite arm during dendritic growth. Therefore, more precipitates were observed in the equiaxed dendrite and columnar dendrite formation regions, in which sufficient time and heat were available for rejection. The quantity of precipitates was decreased in structures similar to cellular growth, and no precipitates were observed in the planar growth region. However, the overall

quantity of precipitates was smaller compared to Alloy 609 when Alloy 709 was used as the filler metal, which can be observed in Figs. 4 and 5. In relation to this, Mu et al. reported that interdendritic precipitates resulted in brittleness and facilitated crack propagation [1, 2]. The difference in shrinkage rate between the γ phase and the precipitates at low temperatures can weaken the bond between the dendrites and the precipitates, resulting in a decrease in low-temperature fracture toughness. It was also noted that the precipitates mostly caused intergranular cracks, and reduced the crack propagation resistance at grain boundaries. They also reported simulation results showing that as the quantity of precipitates increased, concentrated stress, and nearby local plastic deformation increased, resulting in lower toughness [31]. Therefore, the extent of precipitation may affect the low-temperature toughness of the weld metal region. The relatively large quantity of precipitates of Alloy 609 is likely to have a negative effect on toughness. Because Alloys 609 and 709 exhibit no significant microstructural differences other than the precipitates, it is believed that the difference in the absorbed impact energy, which is discussed in Sect. 3.4, results from the formed precipitates. The effect of precipitates on low-temperature toughness requires further investigation in the future.

3.2 Microstructure of transition area of weld joint

Figure 7 shows the composition and phase distribution at the joint interface between the bead and base metal. For

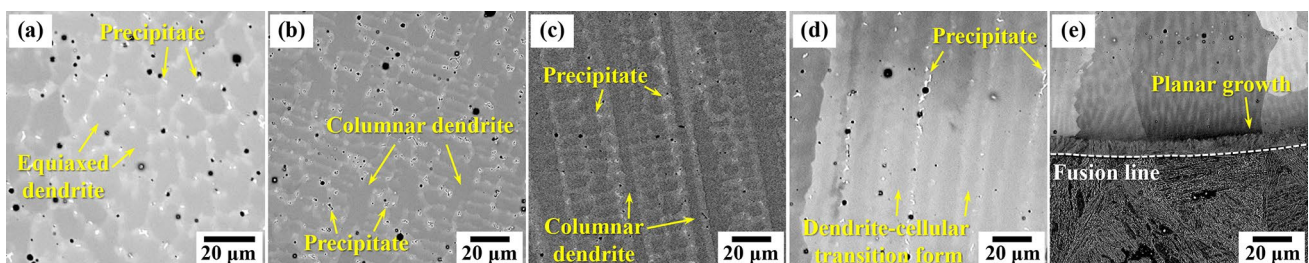


Fig. 5 SEM images with the position within Alloy 609 weld bead. The microstructure in the direction toward the joint interface from bead top is shown in the order of **a** to **e**: weld bead **a** top, **b**, **c** middle, **d** bottom, and **e** joint interface

Table 4 Results of EDS point analysis (wt. %)

Analysis region		Phase	Ni	Cr	Fe	Mo	Mn	W
Alloy 709	Interdendrite	(Mo-rich) γ -phase	55.74	6.68	12.43	19.74	2.93	2.48
	Dendrite	γ -phase	61.01	6.30	14.14	13.87	2.05	2.63
	Precipitate	ρ -phase	34.75	6.60	8.56	44.10	1.62	4.36
Alloy 609	Interdendrite	(Mo-rich) γ -phase	48.28	15.21	18.52	15.64		2.36
	Dendrite	γ -phase	53.35	13.97	20.41	10.08		2.19
	Precipitate	ρ -phase	26.45	13.49	11.72	43.01		5.33

composition distribution, an EDS line analysis was performed along the yellow straight line. In the case of the Alloy 709 weld joint (Fig. 7a), a transition area with linear changes of elements was identified near the fusion line. These compositional changes include decreasing Fe and increasing Ni, Mo, Cr, Mn, and W contents in the direction of the weld metal from the transition area. The phase map indicated that the transition area consisted of two layers, the martensite layer and the γ layer, which was correlated to the γ stabilizer (martensite start temperature (M_s)-decreasing elements). The γ stabilizer includes Cr, Mo, Ni, and Mn. The region containing 10–80 wt% of γ stabilizer forms the γ phase, even with Fe dilution. In contrast, γ cannot become a stable phase in the region with a higher Fe content and transforms into martensite. Furthermore, this region is in contact with the cold base metal and is cooled rapidly, which encourages the transformation to martensite. Similarly, Fig. 7b illustrates the transition area of the Alloy 609 weld joint through dilution. Chen and Lu [32] also reported the formation of the martensite layer at the weld joint interface of low-alloy steel and Inconel 82. In studies by Kim et al. [11], Mu et al. [12], and Dupont and Kusko [33], the martensite layer was observed at the weld joint interface of Fe- and Ni-based alloys. Moreover, the formation of martensite was observed with decreased Cr and Ni contents in an austenitic-ferritic dissimilar welded joint between Fe alloys, indicating the γ stabilizing effect of the elements [34, 35].

The difference depending on the filler metal was manifested in the thicknesses of the martensite and γ layers, which were 13 and 20 μm in Alloy 709, respectively, and 11 and 9 μm in Alloy 609, respectively. The difference in thickness of the transition region can be attributed to the specific heat capacity of the filler metal. The heat required to melt the filler metal differs with the alloy composition. At the same amount of heat input, an Alloy 609 weld joint shows a larger HAZ and deeper penetration depth than those of Alloy 709, in microstructure observation of the weld joint (Fig. 3). From this, it is concluded that more energy is used in the base metal-filler metal mixing in the case of Alloy 609, and less heat is required to melt Alloy 609. In other words, because there is relatively sufficient energy to melt and mix the filler metal and the base metal in the Alloy 609 weld joint, diffusion is facilitated and compositional change can occur at a shorter distance (thin transition layer). Therefore, Alloy 609 exhibits a thin transition region of 20 μm thickness. Furthermore, it is notable that Alloy 709 contains an almost two times thicker γ layer than Alloy 609. This also depends on the contents of the γ stabilizer (M_s -decreasing elements); the martensite finish temperature (M_f) is maintained, while M_s is decreased in regions with a high content of M_s -decreasing elements [12, 33, 36]. Therefore, the temperature range for the martensite transformation decreases, whereas the temperature range for the stable γ phase relatively increases. Therefore, martensite

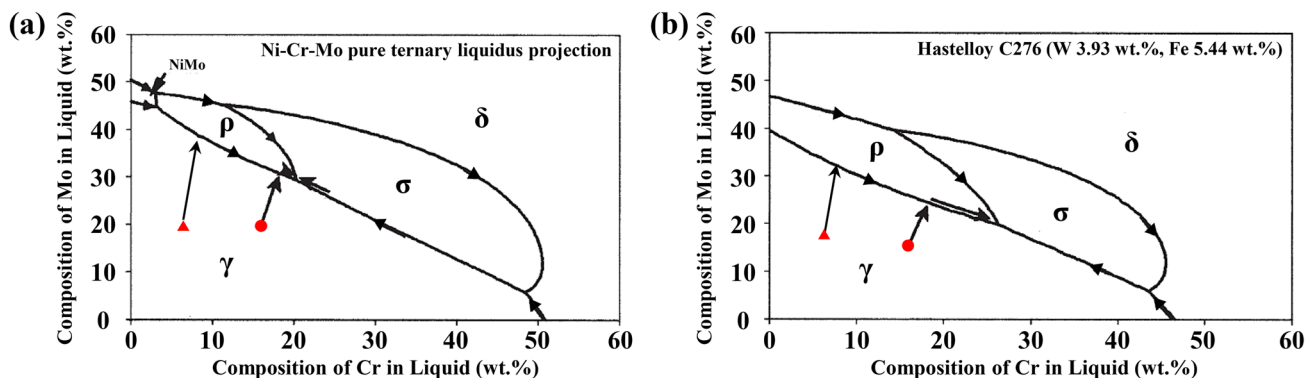
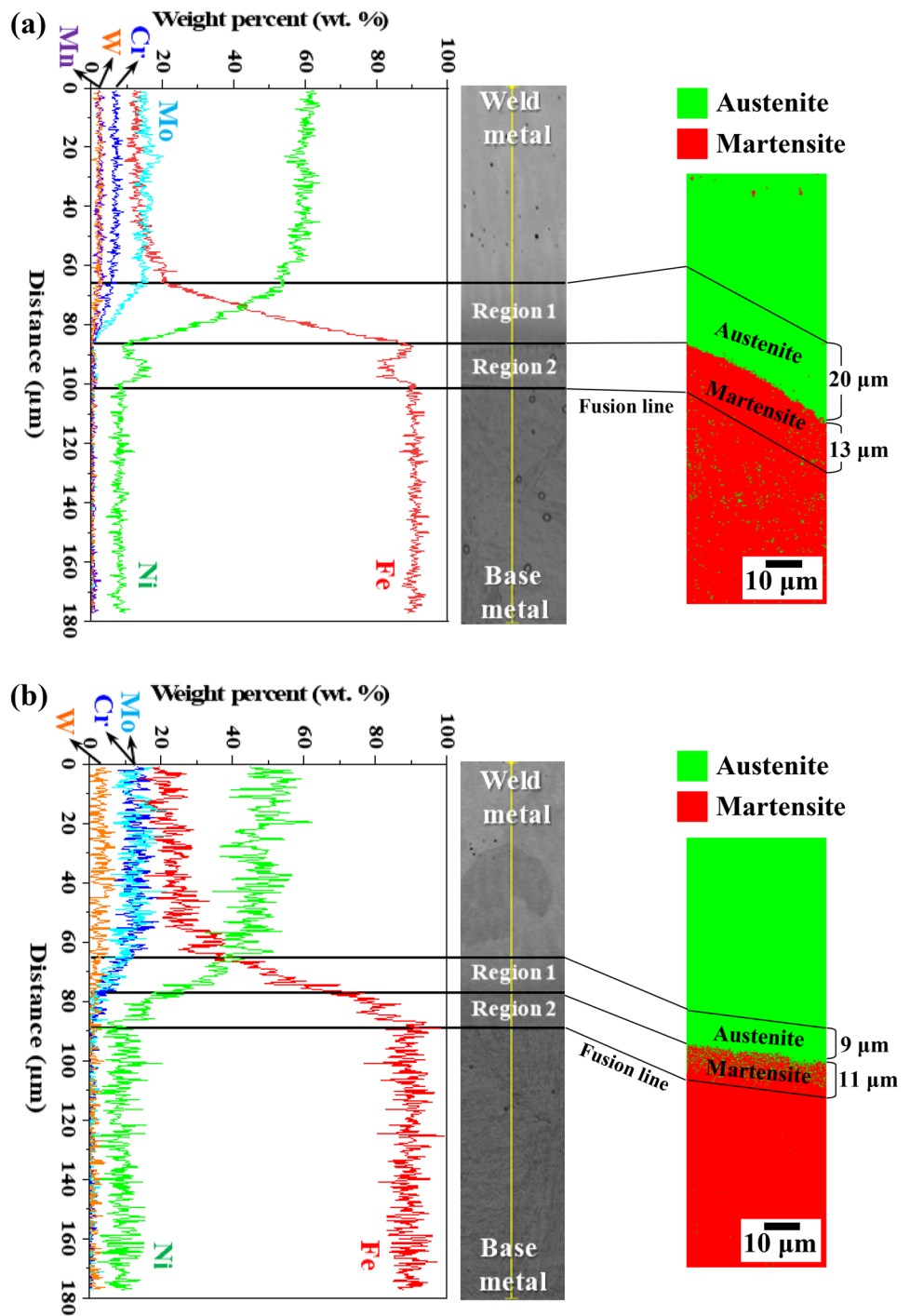


Fig. 6 a Ni–Cr–Mo ternary liquidus projection and b Ni–Cr–Mo ternary liquidus projection according to the addition of Fe and W (black arrows of Alloy 709 are indicated in consideration of the change in Cr

and Mo contents in the interdendritic region from the compositional analysis results) [26]

Fig. 7 EDS line analysis and EBSD results of weld joints made with **a** Alloy 709 and **b** Alloy 609



formation is suppressed while the γ volume fraction increases in regions with a high content of Ms-decreasing elements. As a result, a thick γ layer and a thin martensite layer are formed in the transition area. The comparison of the γ stabilizer content (Ni + Cr + Mo + Mn) in the γ layer indicated a higher γ stabilizer content over a wider interval when Alloy 709 was used, which supported the formation of the thick γ layer and demonstrated the effects of the corresponding elements.

The microstructure and compositional distribution of this transition area of the weld joint can dictate the low-temperature toughness. Two dissimilar alloys are combined at the joint interface, and it may be vulnerable because the weld and base metals vary in microstructure, hardness, and thermal expansion coefficient. In practice, the weld joint can be cooled from room temperature to $-196\text{ }^\circ\text{C}$, and the two alloys would shrink rapidly. During this process, mechanical stress develops at the interface owing to the difference

in the thermal expansion coefficients. In the joint transition area, this stress can cause a phase transformation from γ to martensite. Because martensite has a different lattice constant and crystal structure than γ , the martensite transformation may cause the nearby HAZ to deform, and the residual deformation can result in crack propagation. Therefore, maintaining γ with excellent toughness and without martensite transformation at extremely low temperatures is imperative for low-temperature applications [12]. The γ stabilizer inhibits the martensite transformation, indicating that an interface with a high distribution of γ stabilizer can maintain the γ phase stably at low temperatures while achieving superior low-temperature toughness. Similarly, the structure of the initial transition area with a thin martensite layer and relatively thick γ layer can be advantageous for enhancing low-temperature toughness owing to a small residual deformation. In conclusion, compared to Alloy 609, the microstructure and elemental distribution of the Alloy 709 weld joint resulted in an improved fracture toughness. The superior low-temperature fracture toughness of Alloy 709 is discussed in Sect. 3.4.

3.3 Microstructure of HAZ region

Figure 8 shows SEM images corresponding to each region of the HAZ, where the HAZ is the base metal region affected by heat during the welding process, which manifests below the fusion line. Based on the grain size and phase, the HAZ can be divided into four regions: coarse-grained HAZ (CGHAZ), fine-grained HAZ (FGHAZ), inter-critical HAZ (ICHAZ),

and sub-critical HAZ (SCHAZ) [9, 13]. As shown in Fig. 8a, d, because the CGHAZ is close to the fusion line, it reaches the highest temperature (above A3 temperature) among the four regions and exhibits coarse grains in the grain growth [9, 13]. Because the temperature increases to A3 or higher, the CGHAZ transforms entirely to γ . After the subsequent cooling process, it transforms to coarse martensite lath and coalesced bainite with high strength. In contrast, the toughness of the CGHAZ decreases as the base metal loses its fine grain structure. The CGHAZ is also known to be a major factor in the toughness degradation of the HAZ [13, 37]. The difference in the HAZ region depending on the filler metal was noticeable in this CGHAZ, while similar microstructures were observed in other regions.

Figure 9 shows the cross-section OM images of the CGHAZ directly below the bead (indicated by the red squares in Fig. 3). Coarser grains were observed in the CGHAZ of the Alloy 609 weld joints (Figs. 8a, d and 9), along with a wider CGHAZ region (Fig. 3) compared to Alloy 709, which indicates a higher volume fraction in the region.

Increases in the grain size and volume fraction of the CGHAZ region have a direct effect on the toughness degradation [4]. Therefore, higher toughness was expected in the HAZ when Alloy 709 was used, which was confirmed by the higher absorbed impact energy in the HAZ compared to when Alloy 609 was used. The difference in the microstructure of the CGHAZ with Alloys 709 and 609 is attributed to the specific heat capacity of the filler metal. In this study, the same amount of heat input was provided by the welding

Fig. 8 SEM images of HAZ subzone depending on type of weld metal: **a** CGHAZ, **b** FGHAZ and ICHAZ, and **c** SCHAZ of Alloy 709, and **d** CGHAZ, **e** FGHAZ and ICHAZ, and **f** SCHAZ of Alloy 609

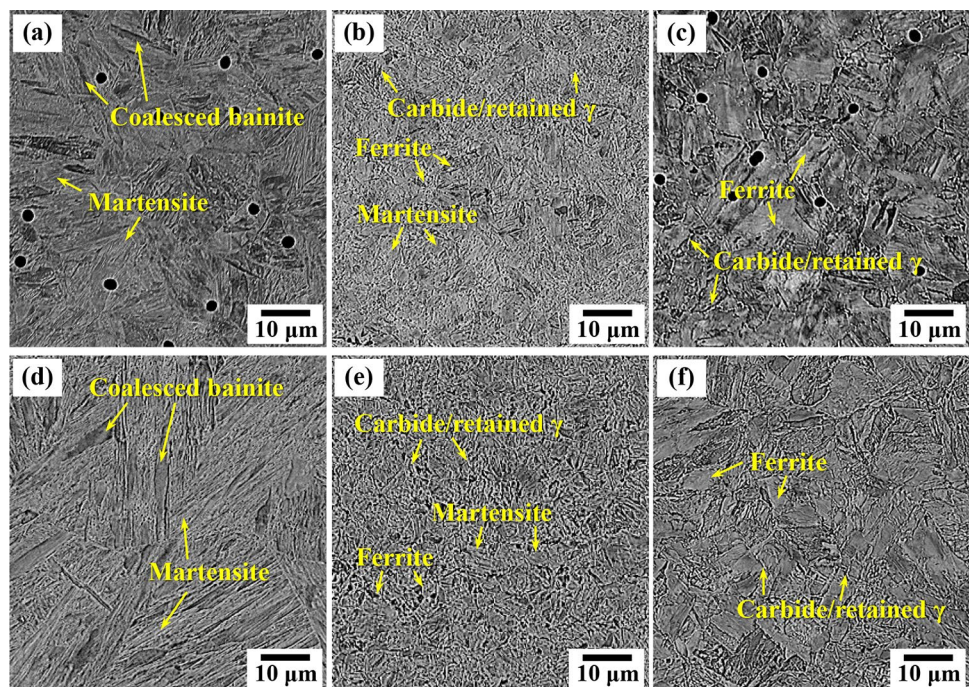
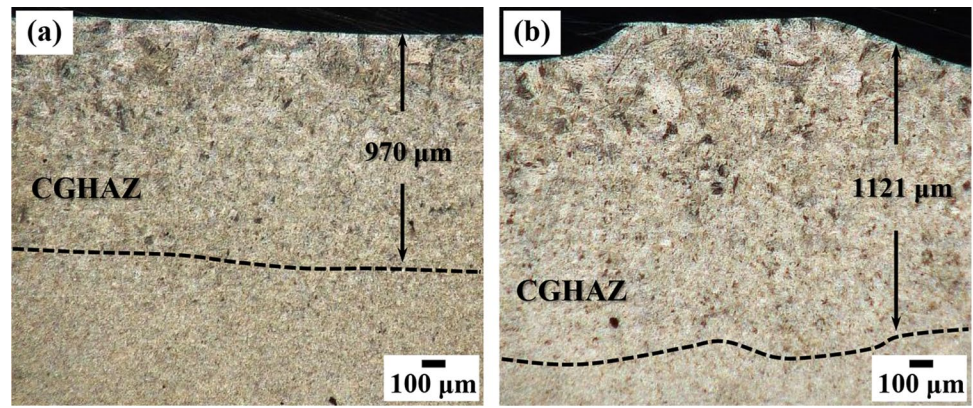


Fig. 9 Cross-sectional OM images of CGHAZ of **a** Alloy 709 and **b** Alloy 609

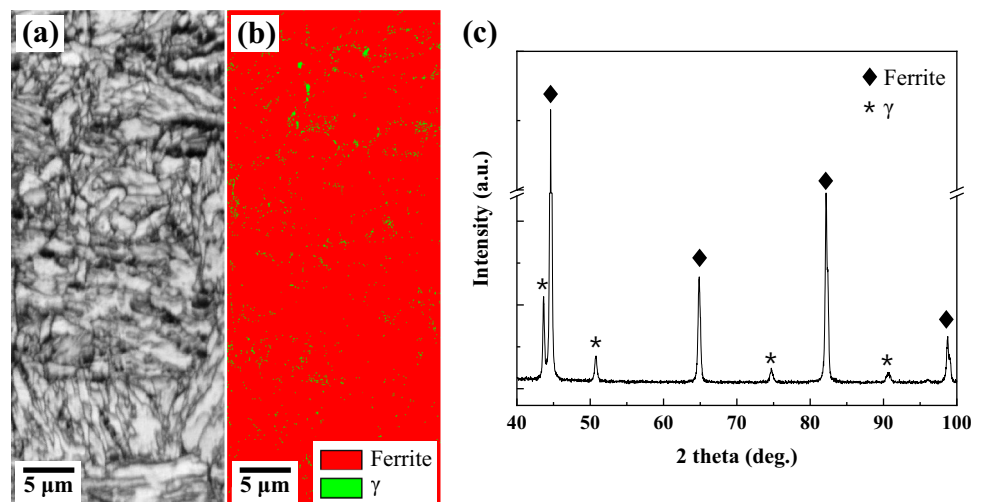


condition; however, the heat capacity required to melt the filler metal depends on the alloy composition. Therefore, the thermal energy transferred to the surrounding base metal differs. If more heat energy is transferred to the base metal, the size of the HAZ can be increased and the grains can be coarsened [38]. Thus, the higher CGHAZ volume fraction and coarser grains in the CGHAZ of the Alloy 609 weld joint indicate that more heat energy is transferred to the base metal under the Alloy 609 bead.

The microstructure in the region below the CGHAZ primarily consists of martensite, and shows fine grains owing to recrystallization (Fig. 8b, e) [9, 13]. The microstructures of the FGHAZ and ICHAZ are determined according to the difference in the reached temperature and the cooling rate with the welding conditions. The FGHAZ is heated to a higher temperature than Ac3, and exhibits a different microstructure depending on the cooling rate after austenitization. Rapid cooling transforms γ into a martensite (majority), some bainite, and carbide/retained γ , whereas relatively slow cooling forms martensite (minority), ferrite, and carbide/retained γ . The ICHAZ is heated to a temperature between Ac1 and Ac3, which partially austenitizes, and then transforms into ferrite and carbide/retained γ with martensite of a different

volume fraction based on the cooling rate. Therefore, the microstructure of martensite, ferrite, and carbide/retained γ can be obtained in the FGHAZ and ICHAZ as in this study, showing a difference in the phase volume fraction. However, such a difference in phase volume fraction could not be clearly distinguished in the microstructure observation, so representative microstructures of the ICHAZ and FGHAZ are shown in Fig. 8b for Alloy 709 and Fig. 8e for Alloy 609, respectively. Deeper in the base metal, no austenitization occurs with a decrease in the heat transfer. Therefore, the volume fraction of ferrite increases, and carbide and the retained austenite appear at the ferrite grain boundary (Fig. 8c, f) [9, 13]. In the study of Passos et al. the ferrite volume fraction in the SCHAZ was about 97.3%, which was reported to be the same as that of the base metal [13]. Similarly, in this study, the ferrite volume fraction of the SCHAZ can be inferred by examining the ferrite fraction of the base metal through XRD and EBSD. Figure 10 shows the results of EBSD and XRD analysis of the base metal. In Fig. 10a and b, the area fraction of ferrite was confirmed to be 98.2%, and the volume fraction measurement using the XRD pattern of Fig. 10c was 97.6%. This indicates the reliability of the analysis results by showing a deviation within 1%.

Fig. 10 EBSD and XRD analysis of the base metal: **a** image quality map, **b** phase map, and **c** XRD result of base metal



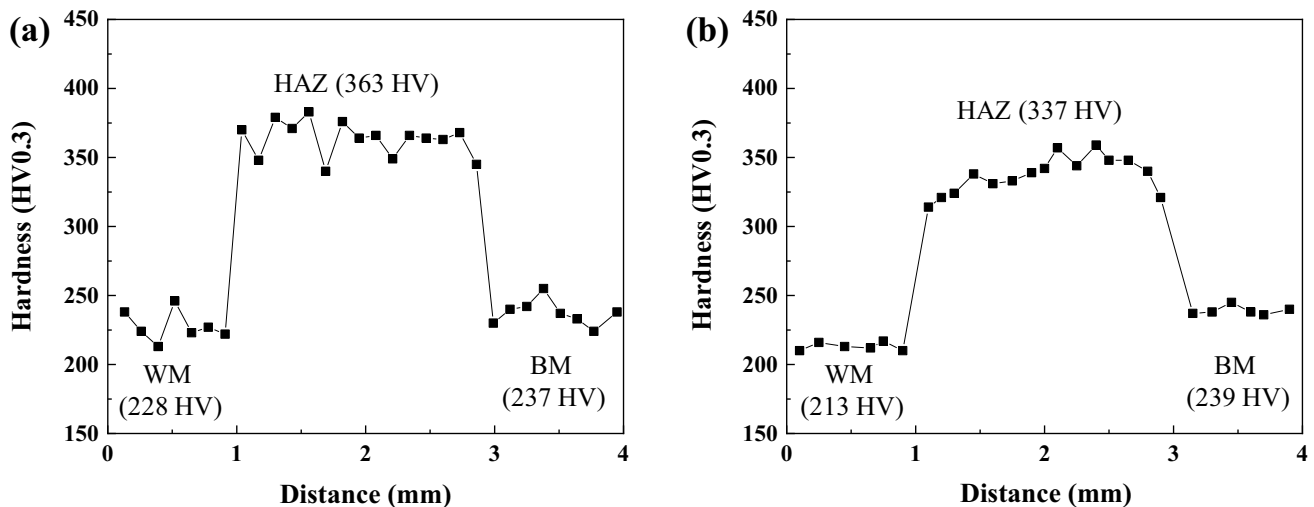


Fig. 11 Vickers hardness results measured in the direction of base metal from weld metal: **a** Alloy 709 and **b** Alloy 609. Average values are shown in parentheses

3.4 Mechanical properties

Figure 11 shows the Vickers hardness results of the weld joint prepared with Alloy 609 and Alloy 709 filler metals. It was measured at regular intervals across the fusion line in the diagonal direction from the weld to the base metal. The trend in the hardness change was identical between the two weld metals. Compared to the weld and base metals, a higher hardness value was obtained in the HAZ region. As martensite with considerable hardness formed in the CGHAZ, FGHAZ, and ICHAZ, the hardness appeared to increase rapidly in the HAZ region. In contrast, because the microstructures of the SCHAZ and base metal were similar, no difference in hardness was observed between them [9, 13]. In the GTAW welding of Inconel 625 performed by Passos et al. [13], the SCHAZ and base metal exhibited a similar hardness value of approximately 225 HV, which is in alignment with the results of this study. Moreover, the maximum hardness value in the ICHAZ was 360 HV, which is similar to the maximum hardness value of the HAZ shown in Fig. 11a, b (Alloy 609, 355 HV; Alloy 709, 375 HV). These high hardness values of the HAZ have also been reported by Kim and Kim in the FCAW welding of ENiMo13T0-1 [39]. However, Alloy 709 achieved a hardness similar to that of base metal in the weld metal region, whereas Alloy 609 exhibited a lower hardness value and was considered to be relatively more vulnerable to damage. It has been reported that the transition region composed of martensite and γ exhibits a hardness value slightly higher than that of the HAZ [12]. As the stress due to martensite transformation in the transition region was transferred to the adjacent γ , high dislocation density was confirmed in the adjacent γ region,

which explained the increase in hardness. In addition, the increase in misorientation due to the stress and the resulting high residual strain contributed to the high hardness. Because the transition region in this study was also composed of martensite and γ layers, an increase in dislocation density and residual strain can inevitably be induced in the surrounding region due to martensite formation. Therefore, it is expected that the transition region can exhibit a hardness comparable to that of the HAZ.

To evaluate the impact toughness at the low temperature of $-196\text{ }^{\circ}\text{C}$, notches were formed in the weld metal, HAZ, and base metal, and the absorbed impact energy was measured (Fig. 2). The results are shown in Fig. 12.

In the weld metal regions of Alloys 609 and 709, the absorbed impact energy was observed to be 55 and 82 J,

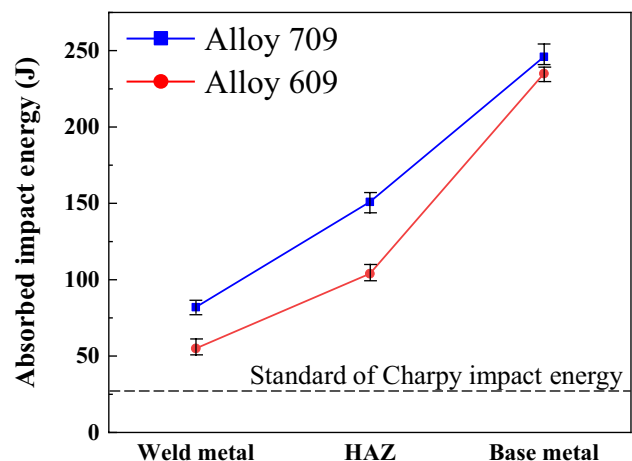


Fig. 12 Results of Charpy impact test performed for weld metal, HAZ, and base metal at $-196\text{ }^{\circ}\text{C}$ (class specification of Charpy impact energy is indicated by dotted line)

Table 5 Impact absorption energy at $-196\text{ }^{\circ}\text{C}$ according to filler metal and welding method

Filler metal	Notch location	Impact absorption energy (J)	Welding method	Reference
Classification regulation on the standard of Charpy impact energy: 27 J in transverse direction				
Average absorbed impact energy of 9% Ni steel used as the base metal: 241 J				
Alloy 709	Weld metal	82	FCAW	Present study
	HAZ	151		
Alloy 609	Weld metal	55	FCAW	Present study
	HAZ	104		
ENiMo13-T	Weld metal	95	FCAW	[43]
	HAZ	138		
Inconel 625	Weld metal	73	FCAW	[19]
	HAZ	166		
ENiCrMo-6	Weld metal	84	SMAW	[19]
	HAZ	139		
Inconel 625	Weld metal	45	SMAW	[44]
ENiCrFe-9	Weld metal	87	SMAW	[45]

respectively, which sufficiently met the class specification [19]. The HAZ exhibited an absorbed impact energy of $> 100\text{ J}$ in both cases, whereas the base metal exhibited the highest value of approximately 240 J . The excellent impact toughness of 9% Ni steel is generally attributed to the refinement of grains and promotion of cross-slip owing to the addition of Ni, resulting in plastic deformation instead of a drastic fracture [40]. Ni also stabilizes the γ phase with high solubility for interstitial elements, including C [40, 41]. Thus, toughness can be improved by inhibiting the formation of precipitates that act as the initiation point for brittle fractures. However, the increased temperature during the welding process results in phase transformation in the HAZ. During this process, the γ volume fraction decreases, and the grains are coarsened, which lowers the absorbed impact energy relative to the base metal. Therefore, a decrease in the thickness of the HAZ region is beneficial for minimizing the initiation and propagation of cracks [42]. Additionally, as mentioned in Sect. 3.3, the low volume fraction and small grain size in the CGHAZ of the Alloy 709 weld joint improve the impact toughness of the HAZ. The result of the impact test of the weld metal region revealed that high absorbed impact energy was obtained with Alloy 709. While the interdendritic precipitates observed in the weld metal result in brittleness and facilitate crack propagation, it is assumed that the impact toughness of Alloy 709 is excellent because it contains a smaller quantity of these interdendritic precipitates. Additionally, in the transition area of the Alloy 709 weld joint, the content of the Ms-decreasing elements (γ stabilizer) is relatively high, and the γ phase can be more stably maintained even in cold shrinkage caused by the low-temperature environment. This suppresses the martensite phase transformation and prevents the formation of residual stress and deformation, which in turn reduces crack initiation and improves toughness [12]. The thin martensite and thick

γ layers in the transition area of the Alloy 709 weld joint also positively affect toughness by maintaining the initial residual deformation at a minimal level. The elemental distribution and microstructure obtained when Alloy 709 was used for welding likely contributed to the improved temperature toughness. Thus, Alloy 709 demonstrated an overall impact toughness superior to that of Alloy 609.

The effects of the microstructure and elemental distribution on low-temperature toughness are summarized as follows:

1. Weld metal: interdendritic precipitate \rightarrow decrease in low-temperature toughness
2. Weld joint: high content of γ stabilizer thin martensite and thick γ layers in the transition area \rightarrow increase in low-temperature toughness
3. HAZ: low CGHAZ volume fraction and fine grain size in the CGHAZ \rightarrow increase in low-temperature toughness

The absorbed impact energy values reported in other studies are listed in Table 5 for comparison; these confirm the applicability of the FCAW welding method. Compared to the SMAW method, which is mainly applied for welding of 9% Ni steel, the weld joint obtained through FCAW also showed comparable high fracture toughness. This shows the feasibility of manufacturing an LNG tank with consistent welding quality by applying FCAW.

4 Conclusions

The microstructures of the weld bead, joint interface, and HAZ of the FCAW joint with 9% Ni steel were investigated for two different Ni-based filler metals, Alloys 709 and 609. The mechanical properties were evaluated accordingly.

Based on the results of this study, the conclusions can be summarized as follows.

1. Based on the crystal growth rate and temperature gradient, the weld bead showed a microstructural transition from planar morphology to equiaxed dendrite. In interdendritic regions, ρ phase precipitates were observed, and a smaller quantity of the precipitates compared to Alloy 609 was confirmed when Alloy 709 was used.
2. The transition region formed by the dilution process consisted of martensite and γ layers, based on the distribution of the γ stabilizers (Ni, Cr, Mo, Mn). The region with a high content of γ stabilizer lowered the martensite transformation starting temperature, suppressed martensite formation, and stabilized the γ phase. This resulted in a transition area consisting of a thick γ layer and a thin martensite layer in the Alloy 709 weld joint.
3. In the microstructure of the HAZ, the CGHAZ directly below the bead clearly demonstrated the effect of using different filler metals. The weld joint with Alloy 709 showed a low CGHAZ volume fraction and fine grains in the corresponding region.
4. In the hardness analysis, the HAZ exhibited higher hardness than the weld and base metals owing to martensite transformation. In the low-temperature Charpy V-notch impact test, the absorbed impact energy was observed to be twice as high as the class specification. When Alloy 709 was used as the filler metal, a better impact toughness was achieved than with Alloy 609. This is considered to happen owing to the following three reasons:
 - Small quantity of precipitates.
 - Stabilization of γ phase owing to high content of γ stabilizer.
 - Low volume fraction and fine grain size in the CGHAZ.

In conclusion, because the weld joint demonstrated a higher absorbed impact energy and excellent low-temperature toughness without degradation of hardness when Alloy 709 was used, this alloy is considered to be a more suitable filler metal for welding 9% Ni steel.

Author contribution Ji Yong Hwang: data analysis, investigation, writing—original draft and revision. Kwangsu Choi: data collection and analysis. Hyo Yun Jung: supervision, review and editing.

Funding This study has been conducted with the support of the Korea Institute of Industrial Technology as research project “PEH22130 [key-tech] localization of 3D printed national defense parts and demonstration support technology development (1/5).”

Declarations

Ethics approval Not applicable.

Consent to participate The submission of the article has been approved by all co-authors.

Consent for publication The publication has been approved by all co-authors.

Conflict of interest The authors declare competing interests.

References

1. Mu W, Li Y, Cai Y, Wang M (2018) Cryogenic fracture toughness of 9%Ni steel flux cored arc welds. *J Mater Process Technol* 252:804–812. <https://doi.org/10.1016/j.jmatprotec.2017.10.026>
2. Mu W, Li Y, Cai Y, Wang M, Hua X (2019) The cryogenic low-cycle fatigue performance of 9% Ni steel joint made by flux cored arc welding. *Mater Charact* 151:27–37. <https://doi.org/10.1016/j.matchar.2019.02.039>
3. Li K, Wang X, Rui SS, Li X, Li S, Sun Q, Zhang Y, Cai Z (2022) Fatigue crack growth mechanism of Ni-based weld metal in a 9% Ni steel joint. *Mater Sci Eng A* 832:142485. <https://doi.org/10.1016/j.msea.2021.142485>
4. Xu T, Shi Y, Jiang Z, Wu L, Ma Y, Wang Z (2022) Improvement of cryogenic toughness for 9% Ni steel keyhole TIG butt-welded joints with a Ni interlayer. *Mater Sci Eng A* 835:142661. <https://doi.org/10.1016/j.msea.2022.142661>
5. El-Batahgy AM, Gumenyuk A, Gook S, Rethmeier M (2018) Comparison between GTA and laser beam welding of 9%Ni steel for critical cryogenic applications. *J Mater Process Technol* 261:193–201. <https://doi.org/10.1016/j.jmatprotec.2018.05.023>
6. Kim JW, Kim JS, Kang SW, Chun KS (2020) Laser welding of ASTM A553–1 (9% nickel steel) (part I: penetration shape by bead on plate). *Metals* 10:484. <https://doi.org/10.3390/met10040484>
7. Berejnoi C, Ipiña JEP (2016) Fracture toughness of ferritic steels in the ductile-to-brittle transition region. In: Alves LM, Ed. *Fracture Mechanics - Properties, Patterns and Behaviours*. IntechOpen, London. <https://doi.org/10.5772/63410>
8. DuPont JN, Lippold JC, Kiser SD (2009) *Welding metallurgy and weldability of nickel-base alloys*. 9% Ni steel, 1st edn. John Wiley & Sons, Inc., New Jersey, pp 357
9. Fernandes VS, Farias FWC, Filho JCP (2020) Fracture toughness of a 9% Ni steel pipe girth welded with Ni-based superalloy 625 filler metal operating in a sour environment. *J Mater Res Technol* 9:6305–6321. <https://doi.org/10.1016/j.jmrt.2020.03.044>
10. Hwang JY, Choi KS, Jung HY (2022) Microstructural evolution and mechanical properties of FCAW joints in 9% Ni steel prepared with two types of Ni-based weld metals. *Int J Adv Manuf Technol* 120:6735–6746. <https://doi.org/10.1007/s00170-022-09173-5>
11. Kim NK, Kang YJ, Bang JH, Song SW, Seo SM, Kang CY, Kang NH (2021) Microstructural evolution and creep behavior of the weld interface between 10% Cr steel and Haynes 282 filler metal. *Metals* 11:764. <https://doi.org/10.3390/met11050764>
12. Mu W, Cai Y, Wang M, Hua X (2020) Microstructure characteristics and properties of fusion boundary in 9%Ni steel joint filled with Ni-based alloy. *Mater Charact* 165:110390. <https://doi.org/10.1016/j.matchar.2020.110390>

13. Passos AV, Farias FWC, Oliveira VHPM, Rios MCG, Filho JCP (2021) Sulfide stress cracking susceptibility of the heat-affected zone of an 9% Ni steel welded joint. *Constr Build Mater* 282:122573. <https://doi.org/10.1016/j.conbuildmat.2021.122573>
14. Oliveira JP, Shamsolhodaei A, Shen J, Lopes JG, Gonçalves RM, Ferraz MDB, Piçarra L, Zeng Z, Schell N, Zhou N, Kim HS (2022) Improving the ductility in laser welded joints of CoCrFeMnNi high entropy alloy to 316 stainless steel. *Mater Des* 219:110717. <https://doi.org/10.1016/j.matdes.2022.110717>
15. Jin Y, Jiahao S, Chenkai G, Yixuan Z, Hongbing L, Oliveira JP, Caiwang T, Zhishui Y (2021) Effect of heat input on interfacial microstructure, tensile and bending properties of dissimilar Al/steel lap joints by laser welding-brazing. *Opt Laser Technol* 142:107218. <https://doi.org/10.1016/j.optlastec.2021.107218>
16. Oliveira JP, Shen J, Escobar JD, Salvador CAF, Schell N, Zhou N, Benafan O (2021) Laser welding of H-phase strengthened Ni-rich NiTi-20Zr high temperature shape memory alloy. *Mater Des* 202:109533. <https://doi.org/10.1016/j.matdes.2021.109533>
17. Martin AC, Oliveira JP, Fink C (2020) Elemental effects on weld cracking susceptibility in $Al_xCoCrCu_yFeNi$ high-entropy alloy. *Metall Mater Trans A* 51:778–787. <https://doi.org/10.1007/s11661-019-05564-8>
18. Jenney CL, O'Brien A (2001) *Welding handbook welding science & technology*. American Welding Society, Miami, Florida
19. Kim BE, Park JY, Lee JS, Lee JI, Kim MH (2020) Effects of the welding process and consumables on the fracture behavior of 9 wt.% nickel steel. *Exp Tech* 44:175–186. <https://doi.org/10.1007/s40799-019-00321-3>
20. Akbari M, Kovacevic R (2019) Closed loop control of melt pool width in robotized laser powder-directed energy deposition process. *Int J Adv Manuf* 104:2887–2898. <https://doi.org/10.1007/s00170-019-04195-y>
21. Kou S (2003) *Welding metallurgy*. John Wiley & Sons, New York
22. Farias FWC, Filho JCP, de Azevedo LMB (2018) Microstructural and mechanical characterization of the transition zone of 9% Ni steel clad with Ni-based superalloy 625 by GTAW-HW. *Metals* 8:1007. <https://doi.org/10.3390/met8121007>
23. Zhu Z, Ma X, Jiang P, Mi G, Wang C (2021) Planar-cellular-dendritic transformation in the fusion zone of a GH909 superalloy weldment. *J Mater Res Technol* 10:960–975. <https://doi.org/10.1016/j.jmrt.2020.12.033>
24. Brito C, Nguyen-Thi H, Manginck-Noël N, Cheung N, Spinelli JE, Garcia A (2019) Cellular-to-dendritic and dendritic-to-cellular morphological transitions in a ternary Al-Mg-Si alloy. *Mater Sci Eng* 529:012018. <https://doi.org/10.1088/1757-899X/529/1/012018>
25. Dong Y, Shuai S, Zheng T, Cao J, Chen C, Wang J, Ren Z (2020) In-situ observation of solid-liquid interface transition during directional solidification of Al-Zn alloy via X-ray imaging. *J Mater Sci Technol* 39:113–123. <https://doi.org/10.1016/j.jmst.2019.06.026>
26. Perricone MJ, Dupont JN, Cieslak MJ (2003) Solidification of Hastelloy alloys: an alternative interpretation. *Metall Mater Trans A* 35:1127–1132. <https://doi.org/10.1007/s11661-003-0132-y>
27. Cieslak MJ, Headley TJ, Romig AD (1986) The welding metallurgy of Hastelloy alloys C-4, C-22, and C-276. *Metall Mater Trans A* 17:2035–2047. <https://doi.org/10.1007/BF02645001>
28. Dupont JN, Lippold JC, Kiser SD (2009) *Welding metallurgy and weldability of nickel-base alloys*. John Wiley & Sons, New Jersey
29. Turchi PEA, Kaufman L, Liu ZK (2006) Modeling of Ni-Cr-Mo based alloys: part I—phase stability. *Calphad* 30:70–87. <https://doi.org/10.1016/j.calphad.2005.10.003>
30. Qiu Z, Wu B, Zhu H, Wang Z, Hellier A, Ma Y, Li H, Muransky O, Wexlera D (2020) Microstructure and mechanical properties of wire arc additively manufactured Hastelloy C276 alloy. *Mater Des* 195:109007. <https://doi.org/10.1016/j.matdes.2020.109007>
31. Mu W, Cai Y, Wang M (2021) Effect of precipitates on the cryogenic fracture toughness of 9%Ni steel flux cored arc weld. *Mater Sci Eng A* 819:141418. <https://doi.org/10.1016/j.msea.2021.141418>
32. Chen ZR, Lu YH (2015) TEM observation of martensite layer at the weld interface of an A508III to Inconel 82 dissimilar metal weld joint. *Mater Sci Eng A* 46:5494–5498. <https://doi.org/10.1007/s11661-015-3171-2>
33. DuPont JN, Kusko CS (2007) Martensite formation in austenitic/ferritic dissimilar alloy welds. *Weld J* 86:51s–54s. <http://files.aws.org/wj/supplement/wj0207-51.pdf>. Accessed 24 Aug 2022
34. Wang Z, Xu B, Ye C (1993) Study of the martensite structure at the weld interface and the fracture toughness of dissimilar metal joints. *Weld J Res Suppl* 72:397–402. https://files.aws.org/wj/supplement/WJ_1993_08_s397.pdf. Accessed 24 Aug 2002
35. Mas F, Tassin C, Roch F, Yescas M, Todeschini P, Bréchet Y (2018) Growth morphologies and primary solidification modes in a dissimilar weld between a low-alloy steel and an austenitic stainless steel. *Metals* 8:284. <https://doi.org/10.3390/met8040284>
36. Hart GLW, Mueller T, Toher C, Curtarolo S (2021) Machine learning for alloys. *Nat Rev Mater* 6:730–755. <https://doi.org/10.1038/s41578-021-00340-w>
37. Jang JI, Ju JB, Lee BW, Kwon DG, Kim WS (2001) Micromechanism of local brittle zone phenomenon in weld heat-affected zones of advanced 9% Ni steel. *J Mater Sci Lett* 20:2149–2152. <https://doi.org/10.1023/A:1013784600394>
38. Yan C, Wu L, Wu W, Yuan Y, Yang X (2019) Prediction of HAZ width in submerged arc welding of mild steel. *IOP Conf Ser Earth Environ Sci* 252:022078. <https://doi.org/10.1088/1755-1315/252/2/022078>
39. Kim JW, Kim JS (2020) Laser welding of ASTM A553–1 (9% nickel steel) (part II: comparison of mechanical properties with FCAW). *Metals* 10:999. <https://doi.org/10.3390/met10080999>
40. Huang G, Wan X, Wu K, Zhao H, Misra RDK (2018) Effects of small Ni addition on the microstructure and toughness of coarse-grained heat-affected zone of high-strength low-alloy steel. *Metals* 8:718. <https://doi.org/10.3390/met8090718>. Accessed 24 August 2022
41. Saitoh N, Yamaba R, Muraoka H, Saeki O (1993) Development of heavy 9% nickel steel plates with superior low-temperature toughness for LNG storage tanks. *Nippon Steel Tech Rep* 9–16. <https://www.nipponsteel.com/en/tech/report/nsc/pdf/5802.pdf>. Accessed 24 Aug 2022
42. Price AH (2013) Significant system parameters influencing HAZ properties in 9%Ni steel. *Sci Technol Weld join* 6:255–260. <https://doi.org/10.1179/136217101101538758>
43. Park JH, Kim YH, Baek HJ, Cho SM (2019) A study on process development of super-TIG welding for 9% nickel steel with Alloy 625. *J Manuf Process* 40:140–148. <https://doi.org/10.1016/j.jmapro.2019.03.017>
44. Filho JCP, Passos EKD, Gonzaga RS, Santos DD, Maia VP, Juliano DR (2020) The influence of the welding process on the ultrasonic inspection of 9%Ni steel pipe circumferential welded joints. *Materials* 13:961. <https://doi.org/10.3390/ma13040961>
45. Wang H, He G (2016) Influence of flux composition on the performance of a nickel-based alloy covered electrode for 9% Ni steel welding. *Weld J* 95:467–478. https://s3.amazonaws.com/WJ-www.aws.org/supplement/WJ_2016_12_s467.pdf. Accessed 24 Aug 2022

Publisher's Note Springer Nature remains neutral with regard to jurisdictional claims in published maps and institutional affiliations.

Springer Nature or its licensor holds exclusive rights to this article under a publishing agreement with the author(s) or other rightsholder(s); author self-archiving of the accepted manuscript version of this article is solely governed by the terms of such publishing agreement and applicable law.